Journal of Materials Chemistry A

ROYAL SOCIETY OF CHEMISTRY

PAPER

View Article Online
View Journal | View Issue

Cite this: J. Mater. Chem. A, 2023, 11, 17759

Pt single atoms dispersed in a hybrid MOFox-in-nanotube structure for efficient and long-term stable photocatalytic H_2 generation†

Shanshan Qin, ‡[a] Junli Guo,‡[b] Xuewen Chen,[ac] Ran Cao,[d] Nikita Denisov,[a] Yan-Yan Song [b] and Patrik Schmuki *[ae]

Received 17th February 2023
Accepted 7th August 2023

DOI: 10.1039/d3ta00996c

rsc.li/materials-a

Atomically dispersed Pt single atoms (SAs) have been reported to be a highly effective co-catalyst on TiO_2 for photocatalytic H_2 generation. Many TiO_2 supports have been explored for hosting Pt SAs. Particularly 1D titania hosts allow for an optimized light and charge carrier management. But, attached Pt SAs often suffer from agglomeration during the photocatalytic process. In this context, titania-based metal–organic frameworks (MOFs), such as MIL-125, have attracted wide attention, as they provide stable anchoring sites for Pt SAs. To combine the beneficial features of the 1D TiO_2 morphology with the SA stability, we introduce here a hierarchical structure, where the Pt SAs are dispersed in MOF-derived porous oxide features that are embedded in aligned anodic TiO_2 nanotubes. This hybrid structure is intrinsically (within the nanotubes) synthesized and combines the excellent light harvesting and carrier transport properties of titania nanotubes with the beneficial features of MOF. As a result of this synergy, we obtain not only a high photocatalytic H_2 evolution efficiency but most importantly a remarkably long-term stability of H_2 evolution under UV light (365 nm) or simulated solar light (AM 1.5).

Introduction

Recently, SAs have attracted a significant interest in photocatalysis where SAs are used as so-called co-catalysts that can strongly accelerate key reactions, such as the photocatalytic splitting of water (photocatalytic H_2 generation[1–3]), the reduction of CO_2 to useable fuels,[4–7] or N_2-fixation (photocatalytic Haber–Bosch process).[8–11]

At the heart of every photocatalytic reaction is a semiconductor that is illuminated with super-bandgap (solar) light. This excitation generates mobile electron–hole pairs that then diffuse or migrate to the semiconductor surface and there initiate desired oxidation and reduction reactions. However, the reaction of photogenerated charge carriers with red-ox species in solution is often kinetically hampered. A prime example of this kinetic hindrance is the photocatalytic H_2 generation on TiO_2 (the most widely investigated photocatalyst in recent science history), where H_2 generation is very sluggish if unmodified titania is used. If TiO_2, and particularly its most active form, anatase, is decorated with so-called co-catalysts, the H_2 production reaction can be accelerated significantly.[12] The co-catalysts are in many cases noble metals (such as Pt, Pd, Rh, *etc.*) deposited in the form of nanoparticles on the light-absorbing semiconductor.[13–15] These co-catalysts act as electron mediator, facilitating efficient electron transfer across the interface and in many cases as a recombination centre for the reaction $2H^0 \rightarrow H_2$. A shrinkage of noble-metal particles to single-atoms is regarded as highly advantageous, not only to maximize the precious metal atom-utilization but also, as scaling down the co-catalyst size bears the prospective of a unique selectivity.[16–18]

However, a crucial issue in all applications of SAs is their high surface energy on many substrates and thus tendency to agglomerate, particularly under illumination during photocatalytic reaction.[19] The most common strategy to prevent agglomeration is to immobilize single atoms in specific structural traps.[20–23] For example, for TiO_2, a number of previous studies reported that SAs could be trapped by appropriate defect sites,[20,24–28] including intrinsic defects in anodic nanotubes,[25,27] or defects created by high temperature reduction of titania.[20,29]

As an alternative, a significantly more effective and stable entrapping of Pt SAs can be reached by anchoring of Pt atoms in

[a]Department of Materials Science WW4-LKO, Friedrich-Alexander-University of Erlangen-Nuremberg, Martensstrasse 7, 91058 Erlangen, Germany. E-mail: schmuki@ww.uni-erlangen.de

[b]College of Sciences, Northeastern University, Shenyang 110004, China

[c]Department of Materials Function and Design, Nagoya Institute of Technology, Gokiso-cho, Showa-ku, Nagoya, Aichi 466-8555, Japan

[d]State Key Laboratory for Modification of Chemical Fibers and Polymer Materials, College of Materials Science and Engineering, Donghua University, Shanghai 201620, China

[e]Regional Centre of Advanced Technologies and Materials, Šlechtitelů 27, 78371 Olomouc, Czech Republic

† Electronic supplementary information (ESI) available. See DOI: https://doi.org/10.1039/d3ta00996c

‡ Shanshan Qin and Junli Guo contributed equally to this work.

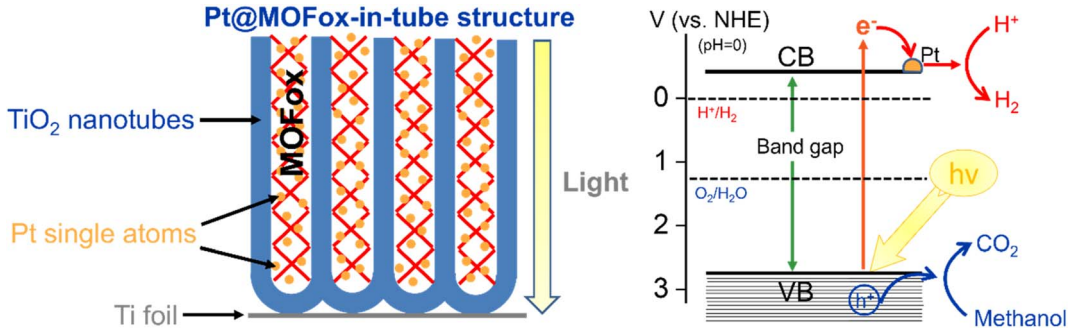

Fig. 1 Schematic depiction of the photocatalytic H_2 evolution scenario by Pt@MOFox-in-tube.

suitable hollow sites of zeolites or metal–organic frameworks (MOFs).[30–35] While SAs can be encapsulated in MOFs, the MOFs can also be converted to porous oxides[36] by post-synthetic oxidation, *i.e.* exposing the MOF to an oxidizing environment, such as oxygen, at high temperatures.

Notably, mesoporous TiO_2 materials synthesized from MOFs can exhibit challenges related to charge carrier conductivity.[36] In contrast to MOF-based TiO_2 structures, 1D titania structures such as self-organized anodic TiO_2-nanotube layers provide strongly advantageous electronic properties with an efficient majority photocarrier transport along the dominant axis and a short diffusion path for minority carriers to the electrolyte.[19,20,24–26,37]

In the present work, we aim to combine the advantages of MOF-structures or MOF-based porous oxide (namely a strong stabilization of SAs) with the advantages of vertically aligned TiO_2 nanotubes (effective charge carrier transport, a high electron mobility, and a highly tunable light absorption path[38–41]). Therefore, we create MIL-125-NH_2 MOF units directly in TiO_2 nanotubes by a simple *in situ* hydrothermal process (MOF-in-tube).[42] After a thermal conversion to oxide, we load the structure with Pt SAs. A schematic is shown in Fig. 1. As a result, for the first time we obtain Pt SA loaded MOF-based oxide-in-tube structure (Pt@MOFox-in-tube). Such a novel hybrid structure significantly outperforms more simple counterparts (Pt SA loaded MOFox or Pt SA loaded nanotubes) in photocatalytic H_2 production, while its high performance is maintained in the long-term owing to enhanced stability of Pt SAs.

Results and discussion

To fabricate Pt@MOFox-in-tube, in a first step, ordered TiO_2 nanotubes (NTs) were grown on a Ti substrate by self-organizing anodization in an ethylene glycol/lactic acid/water electrolyte, as described in the ESI† (Experimental section). Fig. 2a and b show scanning electron microscope (SEM) images of the as-grown TiO_2 nanotube layers. The self-organized nanotube layers are 18 μm thick with individual NTs of 100 nm in diameter. Within these NT layers, we synthesized Ti-MOF-structures by a hydrothermal treatment in a mixture of BDC–NH_2, HCl, CH_3OH and DMF, as described previously.[42] The synthesis is based on the fact that the wall of the as-formed nanotubes consists of amorphous TiO_2 that is mildly soluble under hydrothermal conditions. The solvatized Ti then acts as the Ti source for MOF formation. The amount of MOF is related to amount of solvatized Ti which depends on the residual F^- within the tube structure. The amount of F in grown tubes can be regulated by adjusting the composition of the electrolyte during anodizing. Earlier work showed that TiO_2 tubes prepared from electrolytes with different available F^- contents lead to different MOF loading.[43] In the present study, we used an electrolyte with H_2O content of 2.7 vol% and 0.37% of F^- which leads to 12.3% MOF in tube. After treatment, SEM images (Fig. 2c and d) show typical MIL-125-NH_2 crystals that were formed within the NT layers (Fig. 2d) and also partially on top of the tubes (Fig. 2c).

The fractured tubes in Fig. 2d and S1b† show the high degree of MOF-filling after the hydrothermal synthesis in comparison with MOF-free tubes in Fig. 2b and S1a.† X-ray diffraction (XRD) patterns of as-formed TiO_2 tubes and MOF-in-tube samples (without annealing) are provided in Fig. S2a.† The characteristic diffraction peaks of MIL-125-NH_2 at 9.5° (002), 24.3° (204), and 27.9° (422) found after the reaction of TiO_2 tubes with BDC–NH_2 ligands under hydrothermal conditions confirm the successful formation of MOFs in the TiO_2 tubes. Compared to the XRD pattern of bulk MIL-125-NH_2,[44,45] the MIL-125-NH_2 grown in TiO_2 nanotubes show a reduced crystallinity and a noticeable shift to lower angles. This can be ascribed to the confinement effect of the nanochannels within TiO_2 nanotubes, which leads to a higher content of defects within the MOF nanocrystals.[46] In addition, the appearance of micropores also indicates the growth of MOFs in the TiO_2 nanotubes (Fig. S2b†). However, the synthesized MIL-125-NH_2 within nanotubes also shows the pores of 1–2 nm in size, which are larger than the pore size distribution within MIL-125-NH_2 powder. This can be attributed to the differences in the synthesis process of the above materials – particularly to the effect of solvent acidity during the growth of MOF crystals on the pore size distribution in the resulting materials.[47–49]

MOF formation and loading can be further confirmed by Fourier transform infrared spectroscopy (FTIR) – see Fig. 2e – where after synthesis a characteristic absorption band at 3300–3500 cm^{-1} is obtained that can be assigned to the symmetric and asymmetric stretching vibrations of "–NH_2" groups of BDC–NH_2.[42] In a next step, these MOF-in-tube structures were air-annealed at different temperatures. Temperatures were selected after a thermogravimetric analysis (TGA) of related

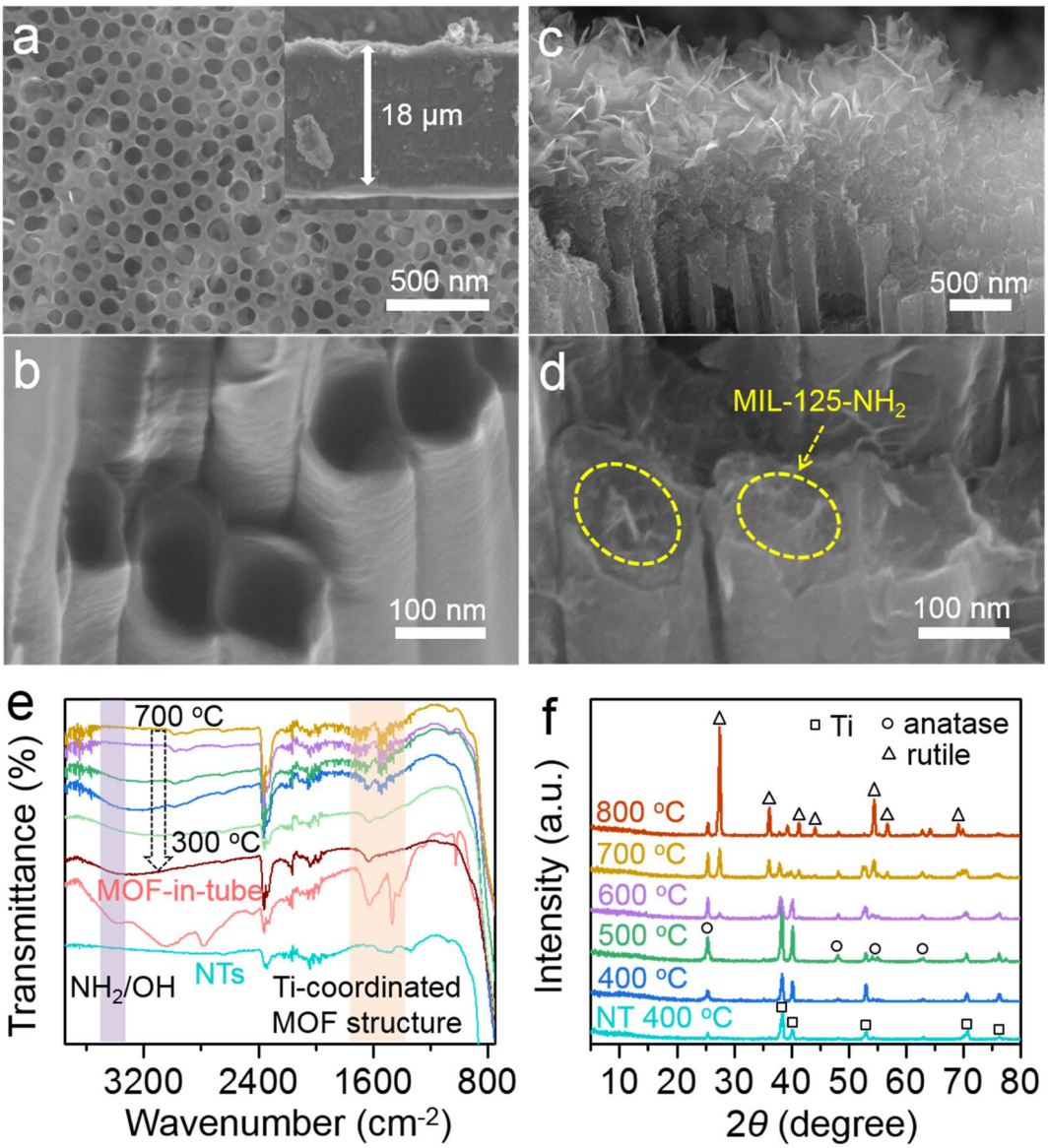

Fig. 2 SEM images of (a and b) TiO_2 NTs and (c and d) MOF-in-tube structure. (e) FTIR of TiO_2 NTs (annealed at 400 °C in air for 2 h) and MOFox-in-tube structures annealed at different temperatures. (f) XRD of MOFox-in-tube structures and TiO_2 NTs annealed at different temperatures.

MOF powders shown in Fig. S3.† The TGA curve of MIL-125-NH_2 exhibits two distinct weight loss features. The first stage is the departure of MeOH and DMF between 25 °C and 300 °C. The second weight-loss stage (between 300 °C and 550 °C) corresponds to the degradation of the BDC–NH_2. Therefore, MIL-125-NH_2 with BDC–NH_2 as linker shows lower thermal stability, starting decomposition at nearly 300 °C.[50,51] Note that the complete removal of the organic linker is reported to be at 400 °C and thus they are completely converted to oxide.[32,50] Accordingly, MOF-in-tube structures were annealed at 400 °C and higher, to reliably obtain MOFox-in-tube structures (Fig. S1c and d†).

In line with TGA, FTIR shows a complete loss of the MOF signature at 300 °C. XRD results (Fig. 2f) show for the MOF-filled and for the plain reference tubes at an annealing temperature of 400 °C a conversion to an anatase structure (see PDF card #21-1272). *I.e.*, at 400 °C, the MOF structure can be converted to a porous oxide structure. This also is in line with experiments conducted on the mesoporous reference bulk MIL-125-NH_2 powder sample (Fig. S4†). Note that the mesoporous nature is confirmed by Brunauer–Emmett–Teller (BET) measurements.[32,50] The BET surface areas of MIL-125 are 174 $m^2\ g^{-1}$, 44 $m^2\ g^{-1}$ and 12 $m^2\ g^{-1}$ for MIL-125 annealed at 400 °C, 500 °C and 600 °C, respectively.[52] *I.e.*, the surface area significantly decreases with the increase of calcination temperature. At temperatures >600 °C for the MOFox-in-tube samples, rutile formation can be observed (see PDF card #21-1276) which also occurs for MOF powder (see Fig. S5†). This is all well in line with the literature on MIL-125-NH_2 that describes a thermolysis and conversion to oxide below 400 °C.[33,42,53]

After annealing, the MOFox-in-tube samples were loaded with Pt SAs using an immersion treatment described previously.[24–26,29]

Then, for all structures, the photocatalytic H_2 production was evaluated in a 50 vol% methanol solution using LED illumination with a power of 65 mW cm^{-2} at a wavelength of 365 nm (Fig. 3a). The results show that non-annealed Pt SA decorated MOF-in-tube structures show hardly any photocatalytic H_2 formation and only after the structure is annealed fully to anatase, a significant activity can be obtained (*i.e.*, for the 400 °C Pt@MOFox-in-tube sample). A mild further increase of the photocatalytic H_2 production is observed for samples annealed at higher temperatures (500 °C, 600 °C, 700 °C) – this slight increase can be ascribed to a higher crystallinity of the samples (see in XRD in Fig. 2f).

However, this activity ranking only holds for measurements performed over shorter periods of illumination (over several hours). If the activity is monitored over 7 days (Fig. 3b), then

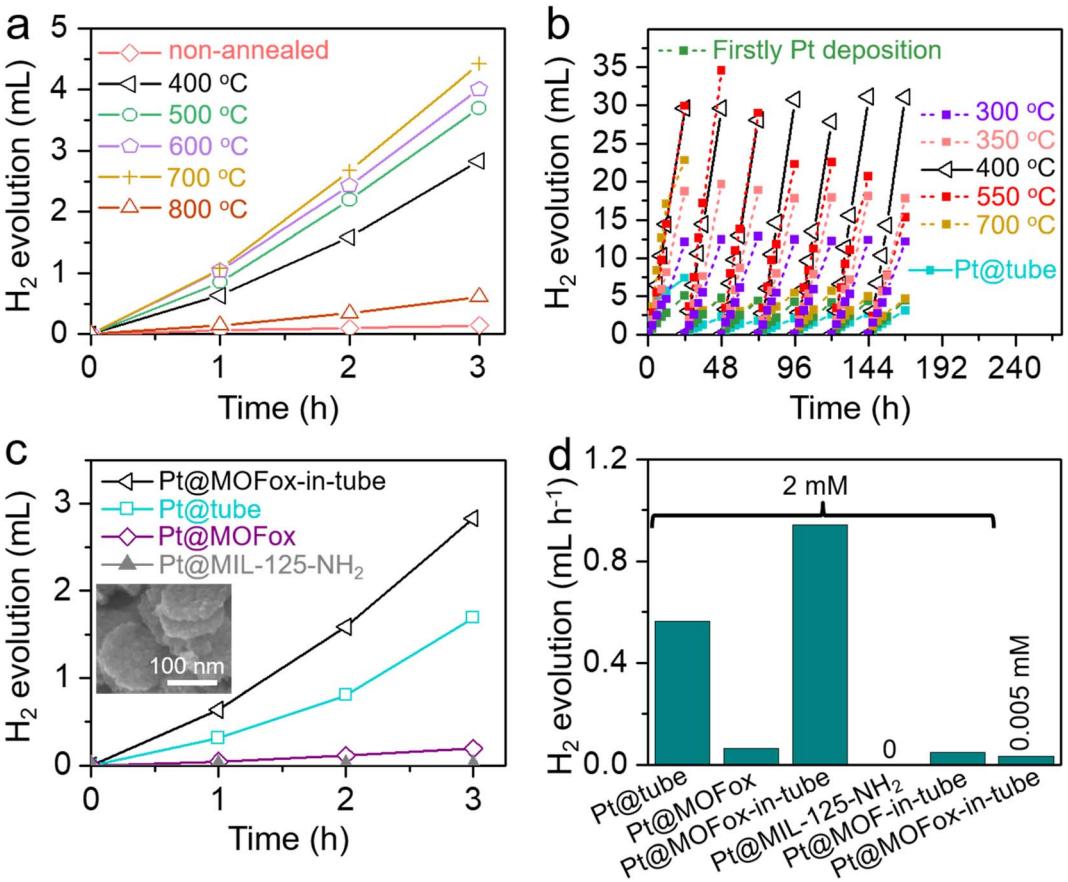

e

Sample name	Pt (at. %) by EDX	Dye loading (nmol cm^{-2})
Pt@MOFox-in-tube (400 °C)	0.54	50
Pt@MOFox-in-tube (550 °C)	0.44	65
Pt@MOFox-in-tube (700 °C)	0.45	26
Pt@MOFox-in-tube (800 °C)	0.05	14
Pt@tube (400 °C)	0.10	36
Pt@MOFox (400 °C)	0.16	-

Fig. 3 (a) Comparison of the open circuit H_2 evolution performance for the Pt@MOFox-in-tube structures annealed at different temperatures and loaded with Pt SAs (2 mM H_2PtCl_6). (b) Long-term photocatalytic H_2 evolution performance for Pt@tube (annealing at 400 °C) and the Pt@MOFox-in-tube structures (annealing at 300–700 °C). "Firstly Pt deposition" refers to Pt@MOF-in-tube structure that was first loaded with Pt SAs, and then annealed at 400 °C. (c and d) Comparison of the open circuit H_2 evolution performance for the Pt@MOFox-in-tube structure (annealing at 400 °C for 2 h), Pt@tube, Pt@MOFox powder and Pt@MIL-125-NH_2 powder prepared by immersion in a 2 mM H_2PtCl_6 solution. In (d), a reference Pt@MOFox-in-tube sample with low Pt SA loading was prepared by immersion in a 0.005 mM H_2PtCl_6 solution. (e) Pt content determined by EDX, and dye loading amounts for Pt@tube and Pt@MOFox powder (annealing at 400 °C) as well as Pt@MOFox-in-tube annealed at different temperatures (Pt SA deposition was performed in 2 mM H_2PtCl_6 solutions).

most remarkable is the long-term photocatalytic H_2 evolution stability for the 400 °C annealed Pt@MOFox-in-tube structure (Fig. 3b and S6a†). It shows 100% retention of the stability of the H_2 evolution rate over the entire test period of 168 h, while other annealing conditions lead to a significant loss of activity over time. Interestingly, the highest initial performance of the 700 °C sample drops already after 24 h below the activity of the sample treated at 400 °C, and 80% of the activity has been lost after 168 h. Additionally, an excellent long-term stability of the photocatalytic H_2 evolution performance by the Pt@MOFox-in-tube structure (400 °C) was also observed under simulated sunlight illumination (AM 1.5), as shown in Fig. S6b.†

To assess the influence of MOFox-in-tube structural synergy on the photocatalytic performance, we compared the data to results for stand-alone MOF-derived or NT structures decorated with Pt SAs (Fig. 3c and d), namely we used: (i) Pt SA-loaded MIL-125-NH_2 powder (Pt@MIL-125-NH_2), (ii) Pt SA-loaded TiO_2 nanotubes (without embedded MOF) (Pt@tube),[25] and (iii) a most popular Pt SA-loaded MOFox powder (Pt@MOFox) from literature[32] (synthesis and details are given in the ESI†). It is worth noting that the photocatalytic MOFox-in-nanotubes, when not decorated with Pt, exhibits minimal H_2 evolution (Fig. S7†).

From the results in Fig. 2a–d, the highest H_2 production rate of 1.472 mL h^{-1} is obtained for the 700 °C annealed Pt@MOF-in-tube structure but also the steady state production rate of the 400 °C sample (0.943 mL h^{-1}) is significantly higher than for free-floating Pt-loaded MOFox (MIL-125-NH_2 annealed at 400 °C) crystallites that yield 0.064 mL h^{-1} – *i.e.* the hierarchical structure outperforms the MOFox-powder by a factor of 23.

The Pt loading from EDX shows for Pt@MOFox-in-tube structures annealed with increasing temperatures a similar loading of ≈0.5 at% Pt (Fig. 3e) until the temperature reached 800 °C (≈0.05 at% Pt) due to a decreased surface area (we will discuss this further below). While the MOFox powder (≈0.16 at%) and the MOF-free tubes show a similar loading of ≈0.1 at% Pt. *I.e.*, the Pt@MOFox-in-tube structures allows for a higher Pt loading of the photocatalyst structure.

Light absorption measurements for the different samples (Fig. S8†) show that the tubes and the MOF-filled tubes (all loaded with Pt SAs) – all show a similar light absorption characteristic – *i.e.*, the presence of MOFox in the nanotubes does not significantly increase the overall light absorption. This can be expected as 18 μm long nanotubes (even unloaded with MOF or Pt) absorb virtually all the useful ($E > E_{gap}$) light.[54]

In order to assess the porosity and specific surface area of the produced hybrid structures, measurements of N_2 adsorption–desorption volumetric isotherms were conducted (Fig. S9a†). The micropore volume within Pt@MOFox-in-tube gradually declines with the increase of calcination temperature (Fig. S9b†). BET surface areas of 173.0 $m^2 g^{-1}$, 136.5 $m^2 g^{-1}$, 81.8 $m^2 g^{-1}$, 46.4 $m^2 g^{-1}$ and 21.5 $m^2 g^{-1}$ were estimated for non-annealed Pt@MOF-in-tube and after annealing at 300 °C, 400 °C, 550 °C and 700 °C, respectively (Fig. S9†). The observed loss of micropore volume and surface area can be attributed to the formation of mesopores within the MOF nanocrystals during the thermolysis treatment, and by the final conversion to TiO_2 and its crystallization.

To directly compare the accessible surface area, we performed dye desorption tests[55] – the results are compiled in Fig. 3e. The accessible surface area for Pt@MOFox-in-tube structures is ≈2-fold higher than for MOF-free tubes, indicating that the presence of MOFox within the tube increases the specific surface area. That the MOF related increase in surface area is not significantly more, is in line with observations in literature that all show that the conversion of a MIL-125 structure to anatase at 400 °C reduces the surface area due to sintering effects, and for higher temperatures an even more drastic loss of surface area occurs in the MOFox.[32,52,53] The tube structure itself (within MOFox-in-tube structure) shows clear sintering at 700 °C and drastically at 800 °C (Fig. S10†) as well as plain TiO_2 nanotube structure (Fig. S11†); this is combined with the loss of surface area and changes in the light absorption characteristics as well as XRD patterns (Fig. S12†).

Overall, the sample annealed at 400 °C shows clearly the best performance over long-term illumination considering all explored conditions. For this sample, after synthesis, high-angle annular dark-field scanning transmission electron microscopy (HAADF-STEM) (Fig. 4a andb) shows the presence of SAs and small SA agglomerates at a density of 2.5 × 10^5 μm^{-2} for Pt SAs and some few-atom agglomerates, "rafts", at a density of 8.5 × 10^4 μm^{-2} for STEM images within the MOFox part of the sample. The 2.4 Å lattice spacing of the substrate is in line with an anatase (004) interplanar distance. Elemental mapping by energy dispersive X-ray spectroscopy (STEM-EDX) confirms a uniform Pt distribution over the entire MOFox-in-nanotube structure (Fig. 4c–e and S13†). In high-resolution SEM (Fig. S14†), no agglomeration is observed for the Pt@MOFox-in-tube samples.

X-ray photoelectron spectroscopy (XPS) of this sample for the XPS Pt 4f region is shown in Fig. 4g, including the corresponding peak fittings. In all cases, Pt is present mainly as surface coordinated (δ^+) single atom $Pt^{\delta+}$ state with $\delta \approx 2$ and $Pt^{\delta+}$ $4f_{7/2}$ at 72.5 eV. This is consistent with our previous works,[25,26,37,56] where we found this chemical shift to correspond to surface trapped oxygen coordinated single Pt atoms.[24,25,29,37] Nevertheless, as reported previously, extended illumination on most TiO_2 structures leads to "light-induced" single atom agglomeration.[19,27,57] According to our previous work,[19] the light-induced destabilization of the surface-anchored Pt SAs can occur due to their interaction with the adsorbed H atoms. As a result, the bonding between Pt SAs and the TiO_2 surface can be sufficiently weakened to allow some Pt SAs to migrate on the surface and aggregate into metallic Pt nanoparticles. Therefore, we compared the best long-term performing Pt@MOFox-in-tube sample, *i.e.* annealed at 400 °C, to the sample annealed at 700 °C after illumination that initially showed the highest H_2 production performance, which however rapidly decayed under illumination.

Agglomeration after illumination indeed is observed for both samples, as directly evident from the SEM images in Fig. 5a and b. However, there are distinct differences: samples annealed at 400 °C show less and much smaller clusters compared to the

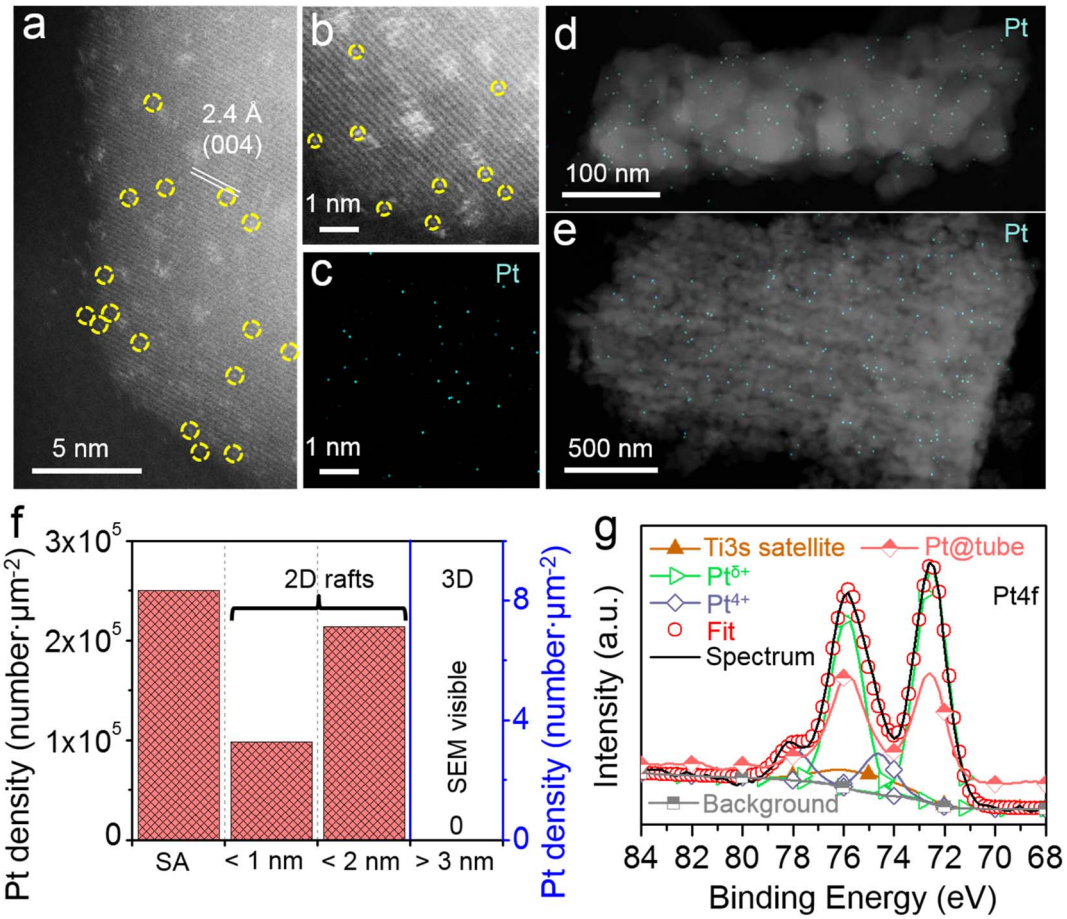

Fig. 4 (a and b) HAADF-STEM images, (c–e) STEM-EDX mapping, (f) statistical size distribution of Pt sites, and (g) XPS spectrum in the Pt 4f region for Pt@MOFox-in-tube structure (annealed at 400 °C in air for 2 h, followed by immersion in a 2 mM H_2PtCl_6 solution).

samples annealed at 700 °C. This is in line with HAADF-STEM taken for the two samples (Fig. 5c, d and S15†) – clearly after illumination still abundant single atom sites on the surface are present; notably with a higher density for the 400 °C sample (1.1×10^5 μm^{-2}) than for the 700 °C sample (7.9×10^4 μm^{-2}). Most notably, very large Pt particles can be detected for the sample annealed at 700 °C. *I.e.*, while samples annealed at 400 °C maintain a much better Pt dispersion, the sample annealed at 700 °C shows Pt agglomerated to much larger cluster sizes (>3 nm).

Fig. 5e gives a quantitative evaluation of the cluster sizes – and again most evident is the agglomeration of Pt to much larger particle sizes for the 700 °C sample and a smaller content of SAs, than for the 400 °C sample (Fig. 5e). Thus, despite an excellent short-term performance by MOFox-in-tube annealed at 700 °C (owing to higher crystallinity), the activity decays due to strong Pt agglomeration. In long-term illumination experiments, the MOFox-in-tube support annealed at 400 °C provides a significantly better dispersion of active centers, which results in a stable H_2 evolution performance. XPS spectra in the Pt 4f region for Pt@MOFox-in-tube structures (400 °C and 700 °C annealed) after 7 days illumination by a 365 nm LED (65 mW cm^{-2}) are shown in Fig. S16.† In line with SEM and HAADF-STEM, after 7 days illumination, more $Pt^{\delta+}$ is detected in 400 °C annealed Pt@MOFox-in-tube structures.

In further experiments we explored some more on the reasons for the beneficial interplay between the MOFox and nanotubes (evident in Fig. 3d). Namely, we compared the electrical and photoelectrochemical properties of individual MOFox samples and nanotube samples with the hybrid MOFox-in-tube structure.

Therefore we acquired incident photon-to-current conversion efficiency (IPCE) spectra (Fig. 6a), transient photocurrent response (Fig. 6b, S17 and S18†), and performed intensity-modulated photocurrent spectroscopy (IMPS) (Fig. 6d and S19†), solid-state conductivity measurements (Fig. 6e), electrochemical impedance spectroscopy (EIS) studies (Fig. S20†), as well as photocurrent decay curves (Fig. 6c).

From the IPCE results (Fig. 6a) most evident is that all MOF-based samples (plain MIL-125-NH_2 or annealed to oxide) clearly show very low photocurrents and IPCE (~1–2%) in comparison to all nanotube-based samples (IPCE > 20%). This reflects the intrinsically inferior electronic properties of MOF (leading to high recombination losses), which improve only slightly after annealing and conversion to anatase (MOFox). After combining the MOFox with the tubes, the MOFox-in-tube sample shows

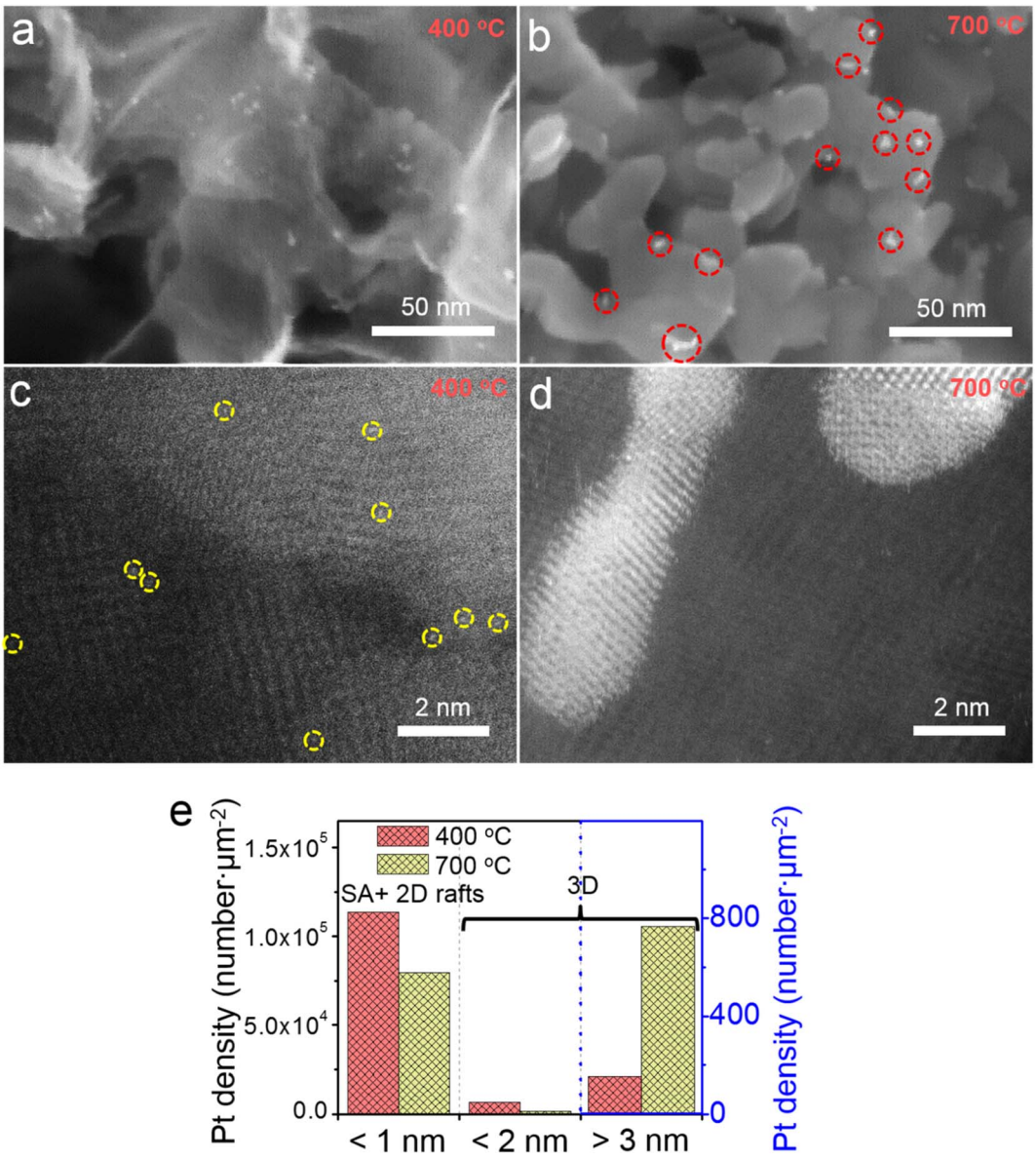

Fig. 5 Characterization of Pt@MOFox-in-tube structures annealed at (a and c) 400 °C and (b and d) 700 °C after photocatalytic H_2 evolution for 7 days under a 365 nm LED illumination (65 mW cm^{-2}): (a and b) SEM images, (c and d) HAADF-STEM images, (e) statistical size distribution of Pt sites.

IPCE approaching that of tubes. It should be noted that nanotubes have an overall much higher electron diffusion length than mesoporous titania structures. In anodic TiO_2 nanotubes the diffusion length of up to 100 μm has been reported,[58] whereas nanoparticulate electrodes show a 4–6 orders of magnitude smaller diffusion length.[38,59,60]

The inferior electronic properties are also evident from simple conductivity measurements in a 2-point setup. Fig. 6e shows current–voltage (*I–V*) curves for the MOFox, the tubes, and the MOFox-in-tube structures. Evidently the tubes and the MOFox-in-tube have very similar conductivity that is clearly higher than that of the MOFox. These results confirm that in such a structure, conductivity is provided by the tubes whereas MOFox have significantly inferior electrical properties.

Additionally, the analysis of transient photocurrent responses (Fig. 6c) and IMPS data (Fig. 6d) confirm these findings. In transient photocurrent plots MOFox-in-tube structures show a faster photocurrent decay (rate constants: $k_1 = 6.36\ s^{-1}$; $k_2 = 0.60\ s^{-1}$), as compared to Pt@tube, Pt@MOFox, and Pt@MOF ($k_1 = 2.22\ s^{-1}$; $k_2 = 0.18\ s^{-1}$). Moreover, the MOFox-in-tube structure exhibits an excellent cycling stability (as depicted in Fig. S18†) with 94% retention of the transient photocurrent response after 10 cycles, whereas the nanotube counterpart only retains 81% of its current density. Non-embedded MIL-125-NH_2 and MOFox powder exhibited only a negligible transient photocurrent (Fig. 6b).

From the IMPS plots in Fig. S19,† MOFox-in-tube shows a higher photocurrent response (*H*), with an approx. 20 times

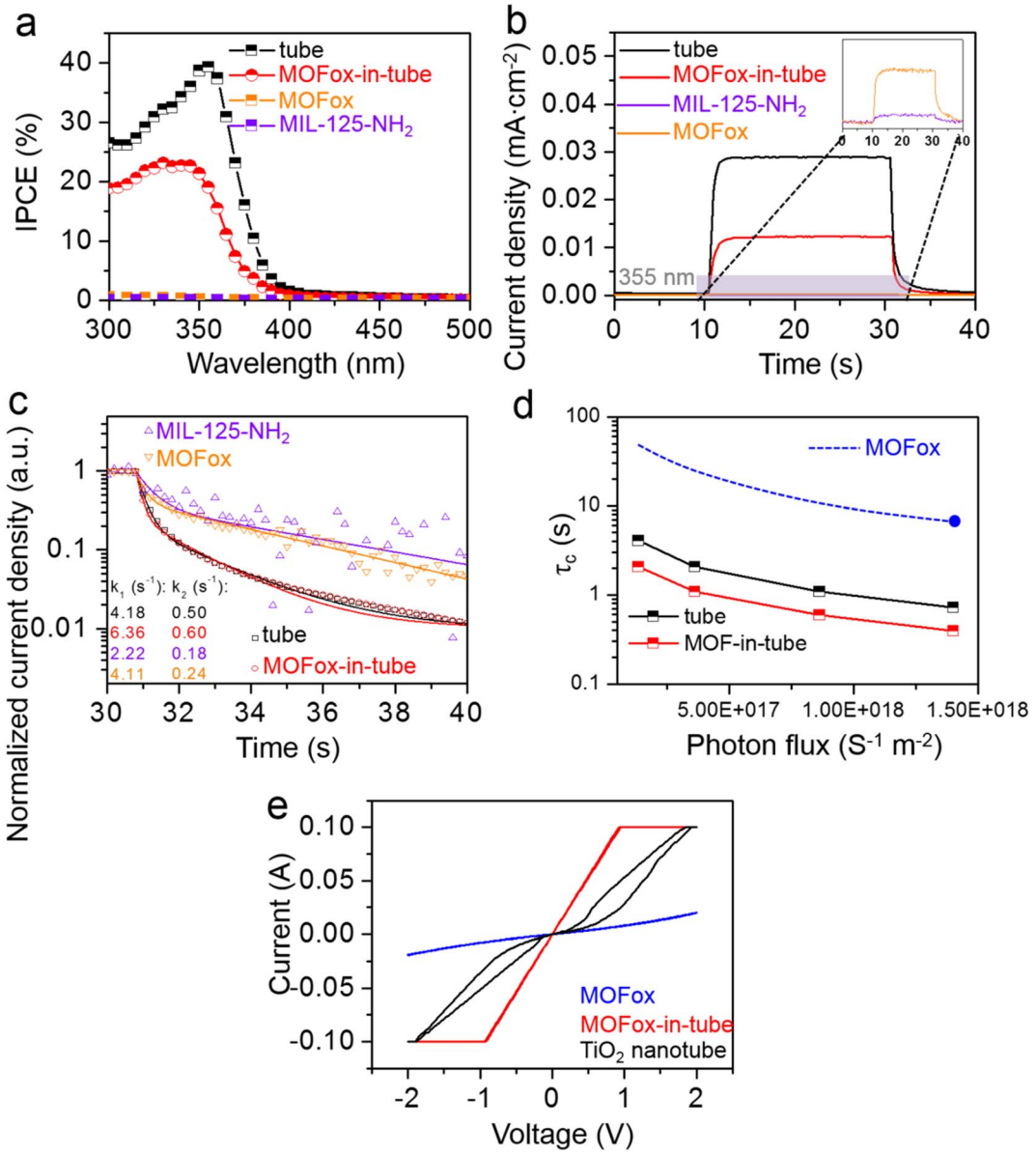

Fig. 6 (a) IPCE spectra, (b) transient photocurrent response, (c) normalized photocurrent decay curves and calculated k_1 and k_2 coefficients (obtained by fitting with bi-exponential function) for the TiO_2 nanotubes ("tube"), MOFox-in-tube structure, MOFox powder and the non-annealed MIL-125-NH_2 powder. (d) Transport time constant (τ_c) values obtained from IMPS plots for MOFox powder, TiO_2 nanotubes ("tube") and MOFox-in-tube structure. (e) Current–voltage curves for MOFox, TiO_2 nanotubes and MOFox-in-tube structure (all samples were annealed at 400 °C).

faster carrier transport constant (τ_c) for the tube-based hybrid structures, as compared to MOFox (Fig. 6d).

EIS studies were conducted to assess the difference in the charge transfer properties and electroactive surface area between the MOFox-in-tube structure and TiO_2 nanotubes. The resulting plots of real *vs.* imaginary impedance (Z_{real} *vs.* $Z_{imaginary}$) and Bode plots are depicted in Fig. S20.† The electrical parameters of both the MOFox-in-tube structure and TiO_2 nanotube were determined through a single time constant (Randles) equivalent circuit model fitting (details are shown in ESI†), and the results are presented in Table S1.† Clearly, MOFox-in-tube structure shows a lower charge transfer resistance (4186.2 Ω cm^2), as compared to TiO_2 nanotube (5893.9 Ω cm^2), in line with higher photocatalytic activity. Considering the space charge layer width to be negligible at $U \approx U_{fb}$, the double layer capacitance (C_{dl}) of the samples can be directly correlated to their electroactive surface area. Based on the estimated C_{dl} values (14 495 μF cm^{-2} and 8798.4 μF cm^{-2}, respectively), MOFox-in-tube structure has 1.65 times higher electroactive surface area than the TiO_2 nanotubes, which is in line with the results of the dye desorption tests (Fig. 3e).

All above results demonstrate that the applicability of stand-alone MOF and MOFox structures is limited by the intrinsically poor photoelectrochemical and electrical properties (leading to

poor photon utilization). Instead, embedding MOFox into the titania tubular structure provides synergistic benefits of the MOFs higher surface area and SA stabilization, with the much better electron transport properties of the tubes. Thus, using MOFox-in-tube structures for anchoring of Pt SAs allows for the most efficient site/photon/carrier utilization in photocatalytic reactions. In other words, not only the pore size and distribution in MOF can impact the charge transport properties, with small pores limiting mass transport and large pores leading to poor electronic conductivity, but also remaining impurities or a large number of grain boundaries detrimentally affect the photoelectrochemical properties. Instead, embedding MOFox into the titania tubular structure provides synergistic benefits of the MOFs higher surface area and SA stabilization, while also benefiting from the much better electron transport properties of the tubes. In addition, these hybrid structures yield a drastically enhanced long-term stability of Pt SAs against photoinduced agglomeration, and thus provide a very long-term stable photocatalyst.

Also, if we compare the results of this work with literature on various TiO_2 nanostructures decorated with SA co-catalysts (such as nanosheets,[19,29,37] nanotubes,[25,27,56] nanoflakes,[26] compact layers[57]), the Pt@MOFox-in-tube structure shows excellent performance (Fig. S21†) that now is combined with a long-term stable photocatalytic H_2 evolution performance.

Conclusions

In the present work we describe Pt SA that are dispersed over a hybrid TiO_2 structure that consists of metal–organic framework (MOF) based porous oxide (MOFox) entities embedded in TiO_2 nanotubes (Pt@MOFox-in-tube structure). For the synthesis of the structure, we modify anatase TiO_2 nanotubes *in situ* with MIL-125-NH_2, oxidize the structure at suitable temperatures, and load the hierarchical structure with Pt SAs. If we evaluate the performance of this Pt@MOFox-in-tube structure for photocatalytic H_2 generation and compare it to the plain Pt@MOFox SA catalysts, we find the hybrid catalyst to be strongly superior, and most importantly it shows a high degree of long-term stability of H_2 evolution under UV light (365 nm) or simulated solar light (AM 1.5). The better performance must be ascribed to the combination of the advantages of the titania nanotube properties (highly adjustable and versatile light and carrier management) with the benefits of the MOF-based structure (stable and strongly dispersed Pt SA).

It is worth noting that MOF only contributes significantly to the activity after its conversion to anatase – nevertheless the converted MOF (MOFox) provides suitable Pt SA anchoring points that provide very high long-term stability. Although partially Pt SAs agglomerated to nanoparticles after photocatalysis, leftover anchored Pt SAs on MOFox-in-tube structure are observed by HAADF-STEM, leading to a high long-term photocatalytic H_2 evolution stability compared with Pt@tube.

In other words, the hierarchical structure introduced here allows to exploit the synergy of the high degree of light and charge carrier management provided by the nanotube architecture with the beneficial entrapping features of SAs in MOFs.

Conflicts of interest

There are no conflicts of interest to declare.

Acknowledgements

The authors would like to acknowledge DFG and the Operational Program Research, Development and Education (European Regional Development Fund, Project No. CZ.02.1.01/0.0/0.0/15_003/0000416 of the Ministry of Education, Youth and Sports of the Czech Republic) for financial support, as well as the support of the Czech Science Foundation projects GA CR-EXPRO, 23-08019X. Zhenni Wu is acknowledged for valuable experimental help. The authors would like to acknowledge the support of the Center for Nanoanalysis and Electron Microscopy (CENEM, Friedrich-Alexander-Universität Erlangen-Nürnberg).

References

1 X. Li, W. Bi, L. Zhang, S. Tao, W. Chu, Q. Zhang, Y. Luo, C. Wu and Y. Xie, *Adv. Mater.*, 2016, **28**, 2427–2431.
2 F. Zhang, Y. Zhu, Q. Lin, L. Zhang, X. Zhang and H. Wang, *Energy Environ. Sci.*, 2021, **14**, 2954–3009.
3 P. Liu, Y. Zhao, R. Qin, S. Mo, G. Chen, L. Gu, D. M. Chevrier, P. Zhang, Q. Guo, D. Zang, B. Wu, G. Fu and N. Zheng, *Science*, 2016, **352**, 797–800.
4 L. Han, S. Song, M. Liu, S. Yao, Z. Liang, H. Cheng, Z. Ren, W. Liu, R. Lin, G. Qi, X. Liu, Q. Wu, J. Luo and H. L. Xin, *J. Am. Chem. Soc.*, 2020, **142**, 12563–12567.
5 Y. Pan, R. Lin, Y. Chen, S. Liu, W. Zhu, X. Cao, W. Chen, K. Wu, W.-C. Cheong, Y. Wang, L. Zheng, J. Luo, Y. Lin, Y. Liu, C. Liu, J. Li, Q. Lu, X. Chen, D. Wang, Q. Peng, C. Chen and Y. Li, *J. Am. Chem. Soc.*, 2018, **140**, 4218–4221.
6 Q. Wang, C. Cai, M. Dai, J. Fu, X. Zhang, H. Li, H. Zhang, K. Chen, Y. Lin, H. Li, J. Hu, M. Miyauchi and M. Liu, *Small Sci.*, 2021, **1**, 2000028.
7 P. Huang, J. Huang, S. A. Pantovich, A. D. Carl, T. G. Fenton, C. A. Caputo, R. L. Grimm, A. I. Frenkel and G. Li, *J. Am. Chem. Soc.*, 2018, **140**, 16042–16047.
8 H. Hirakawa, M. Hashimoto, Y. Shiraishi and T. Hirai, *J. Am. Chem. Soc.*, 2017, **139**, 10929–10936.
9 S. Liu, Y. Wang, S. Wang, M. You, S. Hong, T.-S. Wu, Y.-L. Soo, Z. Zhao, G. Jiang, Q. Jieshan, B. Wang and Z. Sun, *ACS Sustainable Chem. Eng.*, 2019, **7**, 6813–6820.
10 X. Niu, Q. Zhu, S. Jiang and Q. Zhang, *J. Phys. Chem. Lett.*, 2020, **11**, 9579–9586.
11 K. T. Ranjit, T. K. Varadarajan and B. Viswanathan, *J. Photochem. Photobiol., A*, 1996, **96**, 181–185.
12 A. Fujishima, X. Zhang and D. A. Tryk, *Surf. Sci. Rep.*, 2008, **63**, 515–582.
13 Y. Z. Yang, C. H. Chang and H. Idriss, *Appl. Catal., B*, 2006, **67**, 217–222.
14 O. Rosseler, M. V. Shankar, M. K.-L. Du, L. Schmidlin, N. Keller and V. Keller, *J. Catal.*, 2010, **269**, 179–190.
15 J.-J. Zou, H. He, L. Cui and H.-Y. Du, *Int. J. Hydrogen Energy*, 2007, **32**, 1762–1770.

16 B. Xia, Y. Zhang, J. Ran, M. Jaroniec and S.-Z. Qiao, *ACS Cent. Sci.*, 2021, **7**, 39–54.
17 J. Yang, Z. Sun, K. Yan, H. Dong, H. Dong, J. Cui, X. Gong, S. Han, L. Huang and J. Wen, *Green Chem.*, 2021, **23**, 2756–2762.
18 C. Dessal, L. Martínez, C. Maheu, T. Len, F. Morfin, J. L. Rousset, E. Puzenat, P. Afanasiev, M. Aouine, L. Soler, J. Llorca and L. Piccolo, *J. Catal.*, 2019, **375**, 155–163.
19 N. Denisov, S. Qin, J. Will, B. N. Vasiljevic, N. V. Skorodumova, I. A. Pašti, B. B. Sarma, B. Osuagwu, T. Yokosawa, J. Voss, J. Wirth, E. Spiecker and P. Schmuki, *Adv. Mater.*, 2023, **35**, 2206569.
20 S. Hejazi, S. Mohajernia, B. Osuagwu, G. Zoppellaro, P. Andryskova, O. Tomanec, S. Kment, R. Zbořil and P. Schmuki, *Adv. Mater.*, 2020, **32**, 1908505.
21 J. Wan, W. Chen, C. Jia, L. Zheng, J. Dong, X. Zheng, Y. Wang, W. Yan, C. Chen, Q. Peng, D. Wang and Y. Li, *Adv. Mater.*, 2018, **30**, 1705369.
22 H. V. Thang, G. Pacchioni, L. DeRita and P. Christopher, *J. Catal.*, 2018, **367**, 104–114.
23 X. Hu, J. Song, J. Luo, H. Zhang, Z. Sun, C. Li, S. Zheng and Q. Liu, *J. Energy Chem.*, 2021, **62**, 1–10.
24 S. Qin, N. Denisov, B. B. Sarma, I. Hwang, D. E. Doronkin, O. Tomanec, S. Kment and P. Schmuki, *Adv. Mater. Interfaces*, 2022, **9**, 2200808.
25 Z. Wu, I. Hwang, G. Cha, S. Qin, O. Tomanec, Z. Badura, S. Kment, R. Zboril and P. Schmuki, *Small*, 2021, 2104892.
26 G. Cha, A. Mazare, I. Hwang, N. Denisov, J. Will, T. Yokosawa, Z. Badura, G. Zoppellaro, A. B. Tesler, E. Spiecker and P. Schmuki, *Electrochim. Acta*, 2022, **412**, 140129.
27 X. Zhou, I. Hwang, O. Tomanec, D. Fehn, A. Mazare, R. Zboril, K. Meyer and P. Schmuki, *Adv. Funct. Mater.*, 2021, **31**, 2102843.
28 Y. Wang, I. Hwang, Z. Wu and P. Schmuki, *Electrochem. Commun.*, 2021, **133**, 107166.
29 G. Cha, I. Hwang, S. Hejazi, A. S. Dobrota, I. A. Pašti, B. Osuagwu, H. Kim, J. Will, T. Yokosawa, Z. Badura, Š. Kment, S. Mohajernia, A. Mazare, N. V. Skorodumova, E. Spiecker and P. Schmuki, *iScience*, 2021, **24**, 102938.
30 B. Yan, D. Liu, X. Feng, M. Shao and Y. Zhang, *Adv. Funct. Mater.*, 2020, **30**, 2003007.
31 A. Crake, K. C. Christoforidis, A. Kafizas, S. Zafeiratos and C. Petit, *Appl. Catal., B*, 2017, **210**, 131–140.
32 Y. Zhang, J. Zhao, H. Wang, B. Xiao, W. Zhang, X. Zhao, T. Lv, M. Thangamuthu, J. Zhang, Y. Guo, J. Ma, L. Lin, J. Tang, R. Huang and Q. Liu, *Nat. Commun.*, 2022, **13**, 58.
33 T. Wang, X. Tao, X. Li, K. Zhang, S. Liu and B. Li, *Small*, 2021, **17**, 2006255.
34 L. Jiao and H.-L. Jiang, *Chem*, 2019, **5**, 786–804.
35 S. Guo, Y. Zhao, C. Wang, H. Jiang and G. J. Cheng, *ACS Appl. Mater. Interfaces*, 2020, **12**, 26068–26075.
36 X. Zhang, A. Chen, M. Zhong, Z. Zhang, X. Zhang, Z. Zhou and X.-H. Bu, *Electrochem. Energy Rev.*, 2019, **2**, 29–104.
37 S. Qin, N. Denisov, J. Will, J. Kolařík, E. Spiecker and P. Schmuki, *Sol. RRL*, 2022, **6**, 2101026.
38 S. So and P. Schmuki, *Angew. Chem., Int. Ed.*, 2013, **52**, 7933–7935.
39 J. M. Macak, H. Tsuchiya, A. Ghicov, K. Yasuda, R. Hahn, S. Bauer and P. Schmuki, *Curr. Opin. Solid State Mater. Sci.*, 2007, **11**, 3–18.
40 I. Paramasivam, H. Jha, N. Liu and P. Schmuki, *Small*, 2012, **8**, 3073–3103.
41 P. Roy, S. Berger and P. Schmuki, *Angew. Chem., Int. Ed.*, 2011, **50**, 2904–2939.
42 J. Guo, L. Yang, C. Zhao, Z. Gao, Y.-Y. Song and P. Schmuki, *J. Mater. Chem. A*, 2021, **9**, 14911–14919.
43 Z. Dai, J. Guo, C. Zhao, Z. Gao and Y.-Y. Song, *Anal. Chem.*, 2021, **93**, 11515–11524.
44 M. A. Nasalevich, R. Becker, E. V. Ramos-Fernandez, S. Castellanos, S. L. Veber, M. V. Fedin, F. Kapteijn, J. N. H. Reek, J. I. van der Vlugt and J. Gascon, *Energy Environ. Sci.*, 2015, **8**, 364–375.
45 Y. Zhang, J. Guo, L. Shi, Y. Zhu, K. Hou, Y. Zheng and Z. Tang, *Sci. Adv.*, 2017, **3**, e1701162.
46 C. Hu, Y. Bai, M. Hou, Y. Wang, L. Wang, X. Cao, C.-W. Chan, H. Sun, W. Li, J. Ge and K. Ren, *Sci. Adv.*, 2020, **6**, eaax5785.
47 G. Cai and H.-L. Jiang, *Angew. Chem., Int. Ed.*, 2017, **56**, 563–567.
48 Y. Yan, C. Li, Y. Wu, J. Gao and Q. Zhang, *J. Mater. Chem. A*, 2020, **8**, 15245–15270.
49 F. Vermoortele, B. Bueken, G. Le Bars, B. Van de Voorde, M. Vandichel, K. Houthoofd, A. Vimont, M. Daturi, M. Waroquier, V. Van Speybroeck, C. Kirschhock and D. E. De Vos, *J. Am. Chem. Soc.*, 2013, **135**, 11465–11468.
50 L. Feng, S. Yuan, L.-L. Zhang, K. Tan, J.-L. Li, A. Kirchon, L.-M. Liu, P. Zhang, Y. Han, Y. J. Chabal and H.-C. Zhou, *J. Am. Chem. Soc.*, 2018, **140**, 2363–2372.
51 Y. Fu, D. Sun, Y. Chen, R. Huang, Z. Ding, X. Fu and Z. Li, *Angew. Chem., Int. Ed.*, 2012, **51**, 3364–3367.
52 J. Qiu, D. Dai, L. Zhang, M. Li, J. Xu and J. Yao, *Microporous Mesoporous Mater.*, 2021, **319**, 111043.
53 S. Kampouri, C. P. Ireland, B. Valizadeh, E. Oveisi, P. A. Schouwink, M. Mensi and K. C. Stylianou, *ACS Appl. Energy Mater.*, 2018, **1**, 6541–6548.
54 G. Cha, P. Schmuki and M. Altomare, *Chem.–Asian J.*, 2016, **11**, 789–797.
55 A. Elzarka, N. Liu, I. Hwang, M. Kamal and P. Schmuki, *Chem.–Eur. J.*, 2017, **23**, 12995–12999.
56 I. Hwang, A. Mazare, J. Will, T. Yokosawa, E. Spiecker and P. Schmuki, *Adv. Funct. Mater.*, 2022, 2207849.
57 S. Qin, J. Will, H. Kim, N. Denisov, S. Carl, E. Spiecker and P. Schmuki, *ACS Energy Lett.*, 2023, **8**, 1209–1214.
58 J. R. Jennings, A. Ghicov, L. M. Peter, P. Schmuki and A. B. Walker, *J. Am. Chem. Soc.*, 2008, **130**, 13364–13372.
59 S. So, I. Hwang, J. Yoo, S. Mohajernia, M. Mačković, E. Spiecker, G. Cha, A. Mazare and P. Schmuki, *Adv. Energy Mater.*, 2018, **8**, 1800981.
60 M. C. Fravventura, D. Deligiannis, J. M. Schins, L. D. A. Siebbeles and T. J. Savenije, *J. Phys. Chem. C*, 2013, **117**, 8032–8040.

